AFRL-AFOSR-VA-TR-2019-0329

Tailoring Radiative Processes By Nanoengineering For Ultrafast Optoelectronic Devices

Maiken Mikkelsen
DUKE UNIVERSITY

09/09/2019
Final Report

Air Force Research Laboratory
AF Office Of Scientific Research (AFOSR)/ RTB1
Arlington, Virginia 22203
Air Force Materiel Command

REPORT DOCUMENTATION PAGE

Form Approved
OMB No. 0704-0188

1. REPORT DATE *(DD-MM-YYYY)*	2. REPORT TYPE	3. DATES COVERED *(From - To)*
08-11-2019	Final Performance	15 Jul 2015 to 14 Jul 2018

4. TITLE AND SUBTITLE
Tailoring Radiative Processes By Nanoengineering For Ultrafast Optoelectronic Devices

5a. CONTRACT NUMBER

5b. GRANT NUMBER
FA9550-15-1-0301

5c. PROGRAM ELEMENT NUMBER
61102F

6. AUTHOR(S)
Maiken Mikkelsen

5d. PROJECT NUMBER

5e. TASK NUMBER

5f. WORK UNIT NUMBER

7. PERFORMING ORGANIZATION NAME(S) AND ADDRESS(ES)
DUKE UNIVERSITY
2200 W MAIN ST STE 710
DURHAM, NC 27705 US

8. PERFORMING ORGANIZATION REPORT NUMBER

9. SPONSORING/MONITORING AGENCY NAME(S) AND ADDRESS(ES)
AF Office of Scientific Research
875 N. Randolph St. Room 3112
Arlington, VA 22203

10. SPONSOR/MONITOR'S ACRONYM(S)
AFRL/AFOSR RTB1

11. SPONSOR/MONITOR'S REPORT NUMBER(S)
AFRL-AFOSR-VA-TR-2019-0329

12. DISTRIBUTION/AVAILABILITY STATEMENT
A DISTRIBUTION UNLIMITED: PB Public Release

13. SUPPLEMENTARY NOTES

14. ABSTRACT
The overarching research goal of this project is to understand and control light-matter interactions in artificially engineered nanostructures with sub-10 nm dimensions to reveal a new paradigm for ultrafast and large optical responses in the solid state for use in photonic and optoelectronic devices with new or enhanced functionalities

15. SUBJECT TERMS
plasmonics, spontaneous emission, engineered photonic materials, photonics, light-matter interactions, ultrafast, radiative processes

16. SECURITY CLASSIFICATION OF:			17. LIMITATION OF ABSTRACT	18. NUMBER OF PAGES	19a. NAME OF RESPONSIBLE PERSON
a. REPORT	b. ABSTRACT	c. THIS PAGE			POMRENKE, GERNOT
Unclassified	Unclassified	Unclassified	UU		19b. TELEPHONE NUMBER *(Include area code)* 703-696-8426

Standard Form 298 (Rev. 8/98)
Prescribed by ANSI Std. Z39.18

Air Force Office of Scientific Research

Tailoring Radiative Processes by Nanoengineering for Ultrafast Optoelectronic Devices (YIP)

Grant # FA9550-15-1-0301
Program Officer: Dr. Gernot Pomrenke

Principal Investigator: Prof. Maiken H. Mikkelsen, Duke University

Final Report

July 15, 2015 – July 14, 2018

Abstract:

The overarching research goal of this project is to understand and control light-matter interactions in artificially engineered nanostructures with sub-10 nm dimensions to reveal a new paradigm for ultrafast and large optical responses in the solid state for use in photonic and optoelectronic devices with new or enhanced functionalities.

Publications acknowledging AFOSR support:

1) "*Leveraging nanocavity harmonics for control of optical processes in 2D semiconductors*", Gleb Akselrod, Tian Ming, Christos Argyropoulos, Thang Hoang, Yuxuan Lin, Xi Ling, David Smith, Jing Kong & Maiken Mikkelsen, **Nano Letters** 15, 3578–3584 (2015), DOI: 10.1021/acs.nanolett.5b01062

2) "*Ultrafast spontaneous emission source using plasmonic nanoantennas*", Thang B. Hoang*, Gleb M. Akselrod*, Christos Argyropoulos, Jiani Huang, David R. Smith & Maiken H. Mikkelsen, **Nature Communications** 6, 7788 (2015), DOI: 10.1038/ncomms8788

3) "*Large-Area Metasurface Perfect Absorbers from Visible to Near Infrared*", Gleb M. Akselrod, Jiani Huang, Thang B. Hoang, Patrick T. Bowen, Logan Su, David R. Smith & Maiken H. Mikkelsen, **Advanced Materials** 27, 8028-8034 (2015), DOI: 10.1002/adma.201503281

4) "*Colloidal synthesis of nanopatch antennas for applications in plasmonics and nanophotonics*", Thang B. Hoang, Jiani Huang & Maiken H. Mikkelsen, **Journal of Visualized Experiments** 111, e53876 (2016), DOI:10.3791/53876

5) "*Broad electrical tuning of plasmonic nanoantennas at visible frequencies*", Thang B. Hoang & Maiken H. Mikkelsen, **Applied Physics Letters** 108, 183107 (2016), DOI: 10.1063/1.4948588

6) "*Toward Multispectral Imaging with Colloidal Metasurface Pixels"*, Jon W. Stewart, Gleb M. Akselrod, David R. Smith & Maiken H. Mikkelsen, **Advanced Materials** 29, 1602971 (2017), DOI: 10.1002/adma.201770042

7) "*Temporal and spatial valley dynamics in two-dimensional semiconductors probed via Kerr rotation*", Jiani Huang, Thang B. Hoang, Tian Ming, Jing Kong & Maiken H. Mikkelsen, **Physical Review B** 95, 075428, (2017), DOI:10.1103/PhysRevB.95.075428

8) "*Enhanced generation and anisotropic Coulomb scattering of hot electrons in an ultra-broadband plasmonic nanopatch metasurface"*, Matthew E. Sykes, Jon W. Stewart, Gleb M. Akselrod, Xiang-Tian Kong, Zhiming Wang, David J. Gosztola, Alex B. F. Martinson, Daniel Rosenmann, Maiken H. Mikkelsen, Alexander O. Govorov & Gary P. Wiederrecht, **Nature Communications** 8, 986 (2017), DOI: 10.1038/s41467-017-01069-3

9) "*Millimeter-scale spatial coherence from a plasmon laser*", Thang B. Hoang, Gleb M. Akselrod, Ankun Yang, Teri W. Odom & Maiken H. Mikkelsen, **Nano Letters** 17 (11) 6690-6695 (2017), DOI: 10.1021/acs.nanolett.7b02677

10) "*Tailored emission spectrum of 2D semiconductors using plasmonic nanocavities*", Jiani Huang, Gleb M. Akselrod, Tian Ming, Jing Kong & Maiken H. Mikkelsen, **ACS Photonics** 5 (2), 552-558 (2017), DOI: 10.1021/acsphotonics.7b01085

11) "*Surpassing Single-Linewidth Active Tuning with Photochromic Molecules Coupled to Plasmonic Nanoantennas*", Wade M. Wilson*, Jon W. Stewart* & Maiken H. Mikkelsen, **Nano Letters** 18 (2), 853-858 (2018), DOI: 10.1021/acs.nanolett.7b04109

12) "*Probing the origin of highly-efficient third-harmonic generation in plasmonic nanogaps*", Qixin Shen, Thang B. Hoang, Guoce Yang, Viginia D. Wheeler & Maiken H. Mikkelsen, **Optics Express** 26, 20718-20725 (2018), DOI: 10.1364/OE.26.020718

13) "*Extreme nanophotonics in ultrathin metallic junctions*", Jeremy J. Baumberg, Javier Aizpurua, Maiken H. Mikkelsen & David D. Smith, **Nature Materials** 18, 668–678 (2019), DOI: 10.1038/s41563-019-0290-y

Awards and honors received during project period:

Prof. Maiken H. Mikkelsen:

1) Maria Goeppert Mayer Award from the American Physical Society (2017)
2) Early Career Achievement Award, SPIE - international society for optics and photonics (2017)
3) Young Investigator Program (YIP) Award, Office of Naval Research (2017)
4) Young Investigator Program (YIP) Award, Army Research Office (2016)
5) Cottrell Scholar Award, Research Corporation for Science Advancement (2016)
6) Scialog Fellow, Research Corporation for Science Advancement (2016)
7) CAREER Award, National Science Foundation (2015)

Students and postdocs supervised:

1) National Defense Science and Engineering Graduate (NDSEG) Fellowship (Jon Stewart, 2017)
2) Fitzpatrick Foundation Scholar Award, Duke (Andrew Boyce, 2017)
3) Most Outstanding Student Speaker of the Fitzpatrick Institute for Photonics seminar series, Duke (Jiani Huang, 2017)
4) 1st place poster prize, *Southeast Ultrafast conference*, North Carolina State University (Jon Stewart, 2016)

5) 1st place poster prize, *2016 Fitzpatrick Institute for Photonics Symposium*, Duke (Jon Stewart, 2016)

6) NSF Graduate Fellowship, Honorable Mention (Jon Stewart, 2016)

7) Fritz London Postdoctoral Fellowship, Duke (Andrew Traverso, 2016)

8) John T. Chambers Scholar, Fitzpatrick Institute for Photonics, Duke (Jiani Huang, 2015)

9) Pratt-Gardner Graduate Fellowship, Duke (Jon Stewart, 2015)

10) John T. Chambers Fellowship, Fitzpatrick Institute for Photonics, Duke (Jon Stewart, 2015)

Technology transfer:

During the project period, a collaboration with the Connectivity Lab at Facebook (Drs. T. Peyronel and T. G. Tiecke) was established. This collaboration aimed to evaluate the potential of the spontaneous emission rate enhancements observed in nanogap plasmonic structures to be utilized for breakthroughs in free space optical communications. Through this collaboration, the previous demonstrations for large spontenous emission rate enhancements from single nanocavities were extended to practical cm-scale areas. Even over these large areas consistings of thousands of nanocavities, fluorescence enhancements of 910-fold and emission rate enhancements of 133-fold were observed. Additionally, a photon conversion efficiency of 28.6% was measured for these structures showing promise for future practical implementations of these discoveries.
Additionally, a collaboration with Wright-Patterson Air Force Base and Dr. Jarrett Vella was established during the project period. This collaboration was in particular focused on utilizing the multiscale fabrication of the nanogap cavities to achieve future hyperspectral imaging application in a single-shot and on-chip.

Key results:

Below is an overview of the key results obtained during this project.

1) Ultrafast spontaneous emission source using plasmonic nanoantennas

Typical emitters such as molecules, quantum dots and semiconductor quantum wells have slow spontaneous emission with lifetimes of 1–10 ns, creating a mismatch with high-speed nanoscale optoelectronic devices such as light-emitting diodes, single-photon sources and lasers. Here we experimentally demonstrate an ultrafast (<11ps) yet efficient source of spontaneous emission, corresponding to an emission rate exceeding 90 GHz, using a hybrid structure of single plasmonic nanopatch antennas coupled to colloidal quantum dots (**Figure 1**). The antennas consist of silver nanocubes coupled to a gold film separated by a thin polymer spacer layer and colloidal core–shell quantum dots, a stable and technologically relevant emitter. We show an increase in the spontaneous emission rate of a factor of 880 and simultaneously a 2,300-fold enhancement in the total fluorescence intensity, which indicates a high radiative quantum efficiency of ~50% (**Figure 2**). The nanopatch antenna geometry can be tuned from the visible to the near infrared, providing a promising approach for nanophotonics based on ultrafast spontaneous emission.

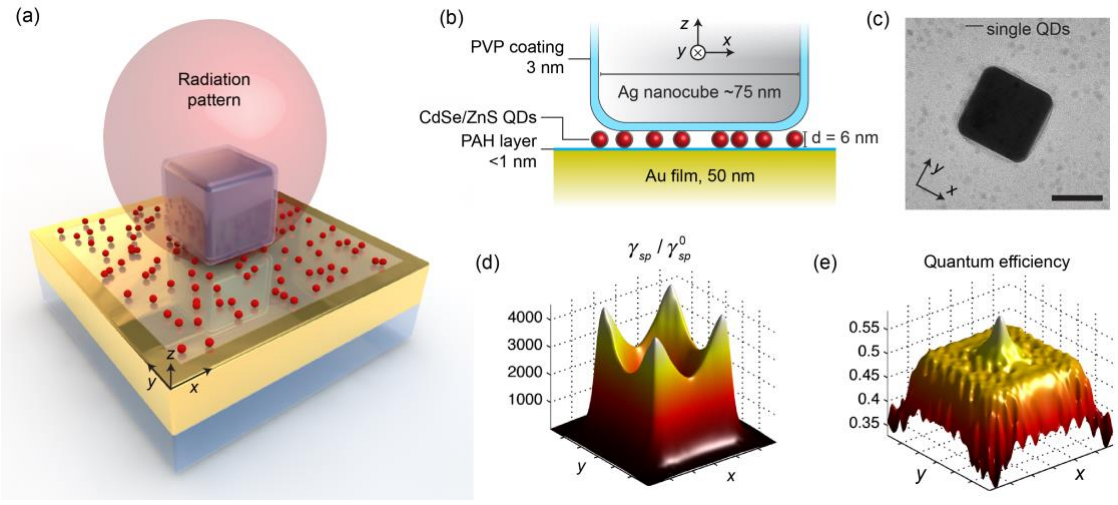

Figure 1. Quantum dots (QDs) coupled to plasmonic nanogap cavities. *(a) Three-dimensional illustration of the plasmonic nanocavity. The simulated directional radiation pattern from the antenna is shown in red. (b) Cross-sectional schematic of the cavity consisting of a silver nanocube on top of an Au film, separated by a 1 nm polyelectrolyte spacer layer and a sparse layer of ~6 nm diameter CdSe/ZnS QDs. (c) Transmission electron microscopy image of a silver nanocube and QDs; scale bar, 50 nm. (d,e) Simulated spatial maps of (d) spontaneous emission rate enhancement (Purcell factor) and (e) radiative quantum efficiency for a vertically oriented QD dipole situated in the gap between the nanocube and the Au film.*

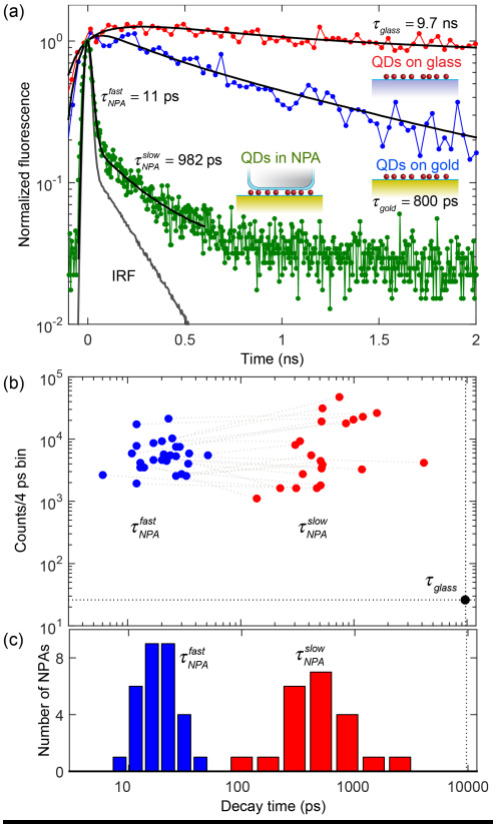

Figure 2. Increased spontaneous emission rate of QDs coupled to plasmonic cavities. *(a) Normalized time-resolved fluorescence of QDs on a glass slide (red) compared with QDs on an Au film (blue) and coupled to a single cavity (green). The instrument response function (IRF) is also shown. Fits to exponential functions convolved with the IRF are shown in black. A single exponential function is used for the QDs on glass and Au. A biexponential function is used to fit the decay of emitters in the cavity. (b) Scatter plot of fluorescence decay times for ~30 cavities showing the relative intensity contributions of the fast and slow decay components. The dashed line connects the two components for each individual cavity. Some decay curves show a more robust fit to a single exponential, and, in these cases, the slow component is not shown. (c) A histogram showing the decay time distribution of the fast and slow components of the ~30 individually measured nanocavities.*

2) Leveraging nanocavity harmonics for control of optical processes in 2D semiconductors

Optical cavities with multiple tunable resonances have the potential to provide unique electromagnetic environments at two or more distinct wavelengths which is critical for control of optical processes such as nonlinear generation, entangled photon generation, or photoluminescence (PL) enhancement. Here, we show a plasmonic nanocavity based on a nanopatch antenna design that has two tunable resonant modes in the visible spectrum separated by 350 nm and with line widths of ~60 nm. The importance of utilizing two resonances simultaneously is demonstrated by integrating monolayer MoS_2, a two-dimensional semiconductor, into the colloidally synthesized nanocavities. We observe a 2000-fold enhancement in the PL intensity of MoS_2 - which has intrinsically low absorption and small quantum yield - at room temperature, enabled by the combination of tailored absorption enhancement at the first harmonic and PL quantum-yield enhancement at the fundamental resonance.

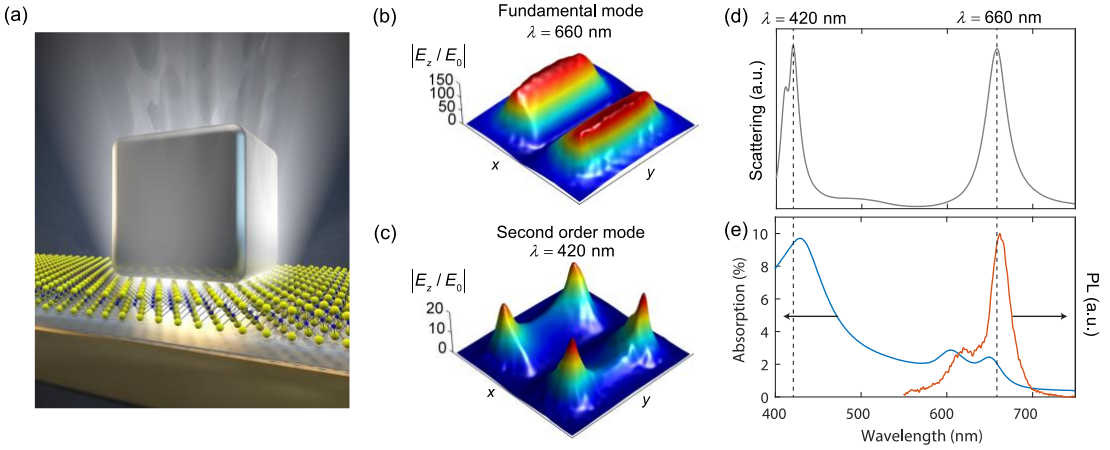

Figure 3. 2D material integrated with nanogap plasmonic cavity. *(a) 3D illustration of the nanocavity, consisting of a silver nanocube over a gold substrate, separated by a monolayer of MoS_2, HfO_2 and polymer layers. (b–c) Spatial maps of the field enhancement across the nanocavity at (b) the fundamental-mode resonance wavelength of λ_p = 660 nm and (c) the second-order mode resonance wavelength of λ_p = 420 nm. (d) Simulated scattering spectrum of a nanocavity, showing the two resonances depicted in b–c. (e) Optical absorption (blue) and PL (red) spectra of monolayer MoS_2 on SiO_2.*

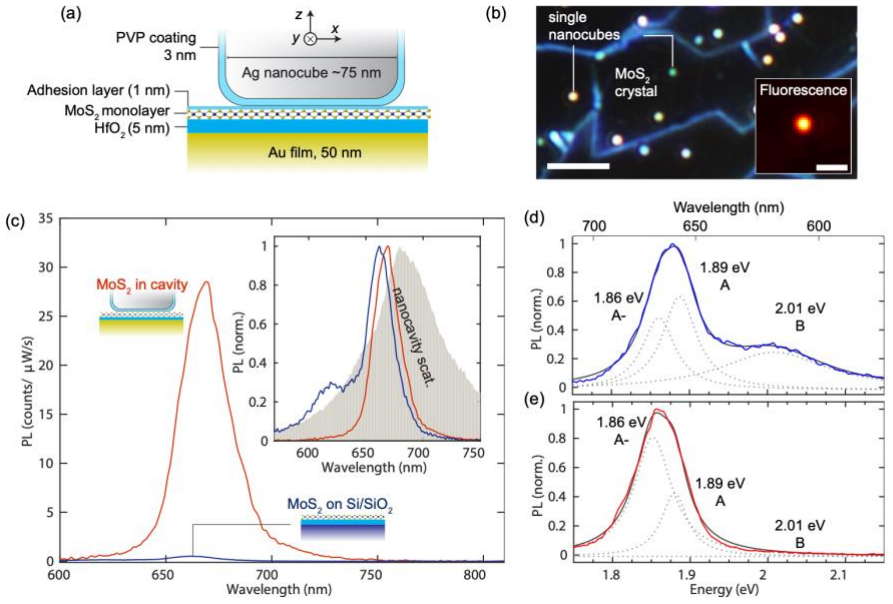

Figure 4. *(a) Cross-sectional schematic illustration of the fabricated nanocavity samples. (b) Dark-field scattering image of the structure, in which the edges of the monolayer MoS_2 crystals appear as blue outlines and individual nanocavities appear as bright spots. The scale bar represents 5 μm. The inset shows a PL image of a different region on the sample obtained under illumination with a defocused laser beam, showing PL from a single nanocavity (bright spot) on monolayer MoS_2. The scale bar represents 1.5 μm. (c) PL spectra from a MoS_2 monolayer on a SiO_2/Si substrate (blue) and in the nanocavity (red). (d and e) Normalized PL spectra from a MoS_2 monolayer on a SiO_2/Si substrate (d) and in the nanocavity (e).*

3) Large-area metasurface perfect absorbers from visible to near infrared

Absorption of light is central to the operation of devices such as photovoltaics, photodetectors, imaging sensors, controlled-emissivity surfaces, and biosensors. Naturally occurring materials either have weak absorption or produce strong reflections, and have poorly defined spectral features beyond the visible spectrum. Nearly perfect absorbers based on metasurfaces with metallic elements have been developed to address these limitations in spectral ranges from the near- infrared to microwave. However, each metasurface element must be deeply subwavelength in size, requiring the use of top-down lithography techniques, inherently limiting their scalability to large areas and for visible spectrum response. In this work, we demonstrate large-area metasurfaces with nearly perfect absorption (99.7%) over truly macroscopic areas using a simple, scalable, and conformal solution-based assembly technique. The metasurface elements are composed of colloidally synthesized silver nanocubes coupled to a metal film (**Figure 5**). The resonance wavelength is easily tunable from the visible to the near-infrared spectrum (**Figure 6**), with the absorbers showing good performance at oblique angles. Given their broad tunability, high efficiency, and good spectral selectivity over a large spectral range, these metasurface absorbers can be integrated with existing technologies for enhanced photodetectors and imaging devices, and for enhanced photocatalysis. The conformal, solution-based deposition (**Figure 7**) also could enable control of absorption and emissivity of surfaces of arbitrary geometry and size.

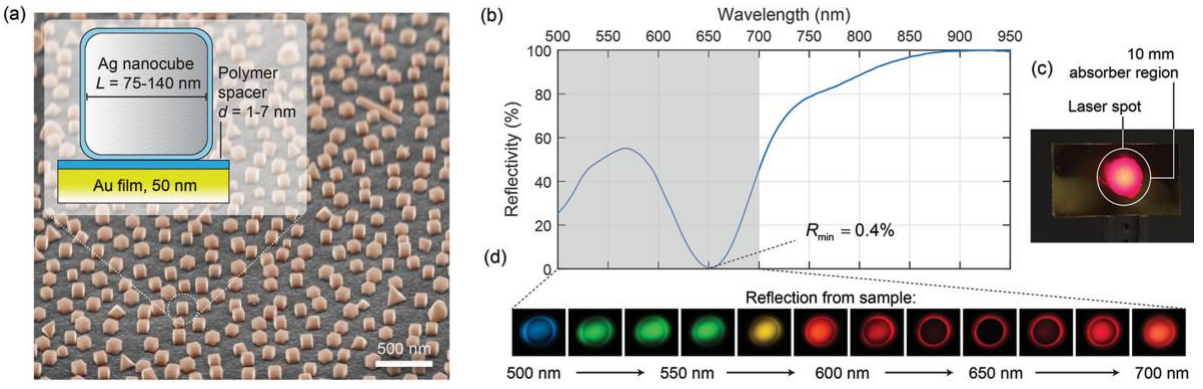

Figure 5. Metasurface perfect absorber based on colloidal silver nanocubes. *a) SEM image of perfect absorber surface consisting of a gold film covered with silver nanocubes. Inset shows cross-section of single subwavelength resonator, in which the gap thickness is controlled by a 1–7 nm polymer layer. b) Reflection spectrum from an absorber with a resonance at 650 nm, utilizing 75 nm nanocubes and a 7 nm spacer, showing a minimum reflectivity of 0.4%. c) Image of sample with a 10 mm region coated with nanocubes on top of gold, while surrounding region is coated only with gold. A defocused laser with a diameter of ≈13 mm illuminates the absorber region. d) Images of the laser beam on a screen after reflection from the absorber sample shown in (c), as the laser wavelength is swept from 500 to 700 nm. When the laser is resonant with the absorption at 650 nm, no reflection is seen from the nanocube coated region.*

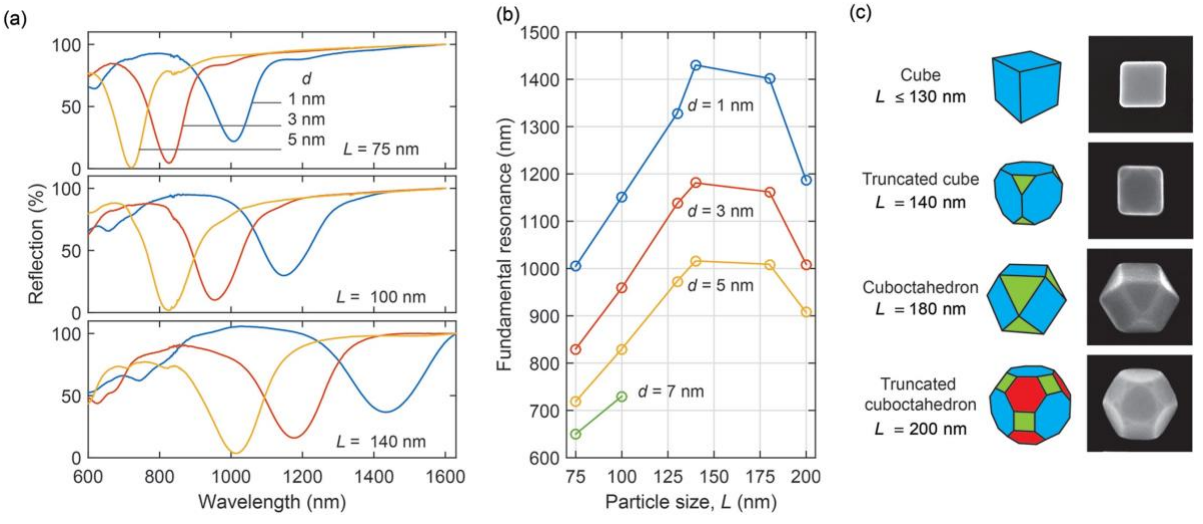

Figure 6. Tuning the absorber resonance from visible to near-infrared. *a) Reflection spectra of absorbers with resonances from the visible to the near-infrared using a range of nanocube sizes (L) and spacer layer thicknesses (d). b) Resonance wavelength as a function of particle size and spacer thickness. c) SEM images of typical particles from each synthesis having average particle size L. For L ≥ 140 nm the particles become noncubic, transitioning to a truncated cube, to a cuboctahedron, to a truncated cuboctahedron. As the particle size increases, the facets become smaller, blueshifting the absorber resonance, seen in (b).*

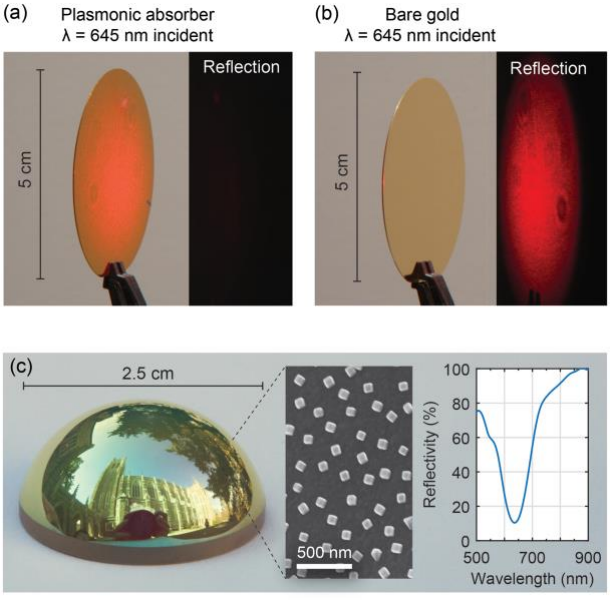

Figure 7. Large area and conformal absorber. *a) A 5 cm diameter wafer coated over the entire surface with a gold film, a 7 nm spacer, and 75 nm nanocubes, with a resonance of 645 nm. A defocused 645 nm laser beam is incident on the sample and the reflection is imaged on a screen, showing almost no visible reflection. b) For comparison with (a), a 5 cm wafer coated only with a gold film shows strong reflection of the laser beam, imaged using the same camera exposure settings. c) A glass half-sphere coated with 100 nm of silver and a 7 nm polymer spacer layer, followed by conformal deposition of 75 nm nanocubes. Insets show SEM image taken on the side slope of the sample, and the near-normal incidence reflectance spectrum.*

4) Multiscale fabrication of nanogap plasmonic structures.

Multispectral infrared (IR) imaging, an amalgamation of imaging and spectroscopy, is a critical tool for chemical and thermal sensing applications such as monitoring environmental pollutants, detecting cancerous tissues, and inspecting produce. Despite the potential impact of multispectral technologies, its widespread usage has been significantly hindered by the complex scanning optical systems required. A promising approach to bypass this issue is to replace the scanning optical systems with multispectral focal plane arrays, composed of spectrally selective pixels. However, the poor spectral selectivity of naturally occurring materials beyond the visible spectrum makes the fabrication of spectrally selective pixels exceedingly challenging. Recently, metasurfaces consisting of subwavelength plasmonic resonators have demonstrated strong and spectrally selective absorption in the shortwave IR wavelengths, promising for the realization of multispectral optoelectronics. However, to date plasmonic pixels or metasurfaces have been unable to simultaneously achieve narrow spectral selectivity, strong absorption, and scalable fabrication in the visible to near IR regimes. Here we demonstrate metasurface pixels exhibiting greater than 85% absorption and ≈100 nm spectral widths by patterning plasmonic resonators in micrometer-scale pixels using a fusion of bottom-up and top-down fabrication techniques over wafer-scale areas (**Figure 8**). The plasmonic resonators, tuned from 580 to 1125 nm, are composed of colloidally synthesized silver nanocubes separated from a gold film with a 4–10 nm spacer layer. To display the capability of this technique, we fabricate a multispectral metasurface pixel array consisting of six resonances and reconstruct a red, green, and blue (RGB) image with a combinatorial pixel scheme exhibiting 9261 color combinations (**Figure 9**).

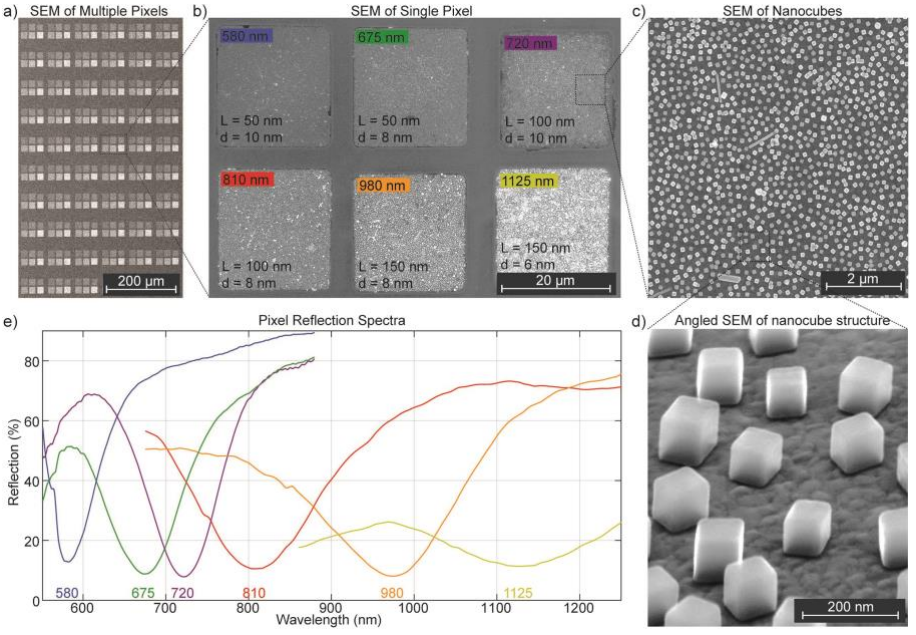

Figure 8. Multispectral pixel array*. a) SEM image of multiple pixels showing the uniformity of patterning. b) SEM image of a single pixel labeled according to their corresponding spectrums. The nanocube size, L, and the gap thickness, d, are labeled for each resonance. c) SEM image of the uniform distribution of cubes within the 20 µm × 20 µm squares. d) Angled SEM image showing silver nanocubes (L = 75 nm) on a gold substrate. e) Spectrum of six different plasmonic resonances across the visible to near infrared patterned on a single substrate.*

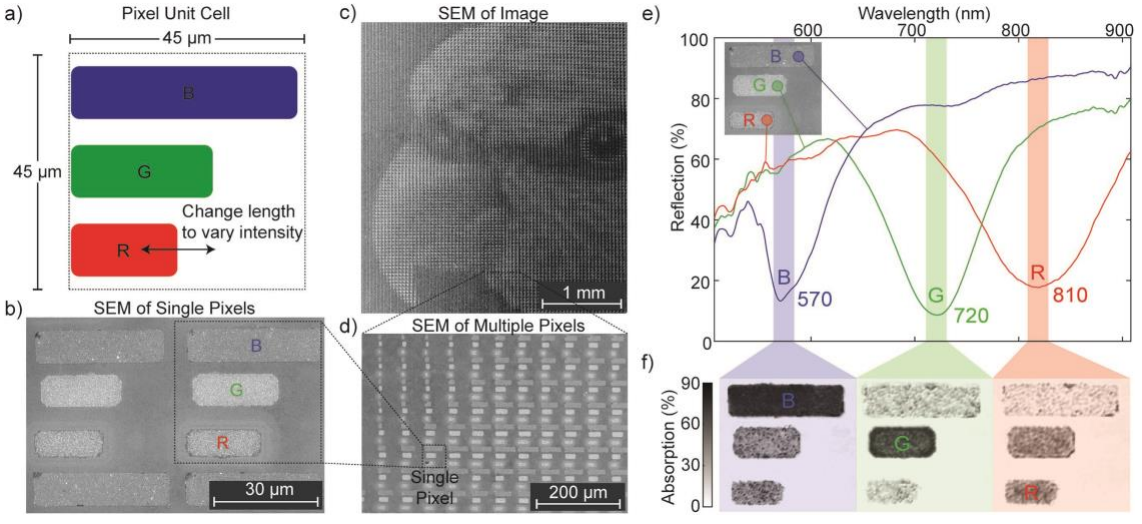

Figure 9. Nanocube RGB pixel structure. *a) Diagram of the pixel unit cell used to reconstruct an RGB image with the nanocube absorbers. The intensity of each color is tuned by varying the length of the rectangles in 2 µm increments. b) SEM image depicting actual pixels of the reconstructed RGB image. c) SEM image showing pixels with varying rectangle lengths along edge of parakeet head. d) SEM image of the parakeet head. e) Spectrum of three different colors used to reconstruct the RGB image. f) Images of pixels taken with ±10 nm bandpass filters around each resonance.*

5) Broad electrical tuning of plasmonic nanoantennas at visible frequencies

We report an experimental demonstration of electrical tuning of plasmon resonances of optical nanopatch antennas over a wide wavelength range. The antennas consist of silver nanocubes separated from a gold film by a thin 8 nm polyelectrolyte spacer layer. By using ionic liquid and indium tin oxide coated glass as a top electrode, we demonstrate dynamic and reversible tuning of the plasmon resonance over 100 nm in the visible wavelength range using low applied voltages between -3.0 V and 2.8 V (**Figure 10 and 11**). The electrical potential is applied across the nanoscale gap causing changes in the gap thickness and dielectric environment which, in turn, modifies the plasmon resonance. The observed tuning range is greater than the full-width-at-half-maximum of the plasmon resonance, resulting in a tuning figure of merit of 1.05 and a tuning contrast greater than 50%. Our results provide an avenue to create active and reconfigurable integrated nanophotonic components for applications in optoelectronics and sensing.

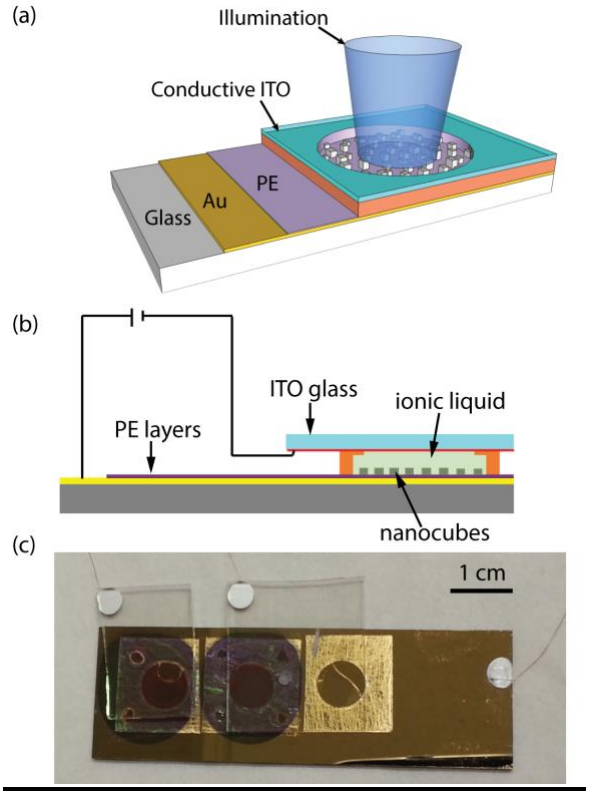

Figure 10. Device structure for electrical tuning of plasmon resonances. *(a) Schematic of the sample design consisting of silver nanocubes separated from a gold film by a thin polyelectrolyte (PE) spacer layer. An approximately 1 cm^2 area of the sample is isolated using spacer tape, creating a circular opening filled with an ionic liquid and subsequently covered by an ITO coated glass slide. (b) Schematic cross-section of the sample structure is shown including electrical contacts. (c) Photograph of a fabricated structure with three devices. The spacer tape containing ionic liquid within the circular openings is seen along with the ITO coated slides used for electrical contacts. The two devices on the left consist of the structure as illustrated in (a) and (b), whereas the right device is the same structure but without any nanocubes and is used for normalization purposes.*

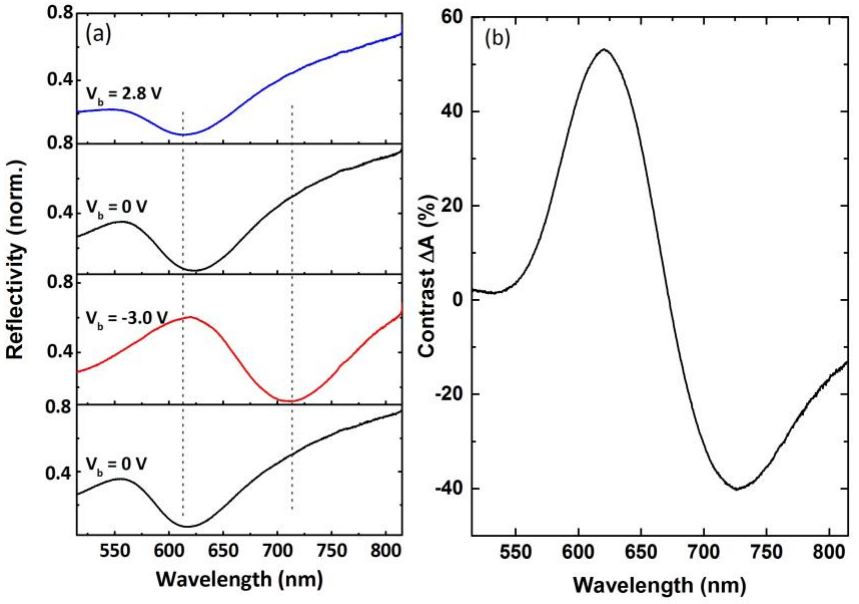

Figure 11. Dynamic tuning of the plasmon resonance. *(a) Reflectivity spectra of an ensemble of nanopatch antennas measured at different applied bias voltages, V_b, as indicated. The experimental sequence performed is shown from the top to the bottom panel. The dashed lines indicate the 100 nm tuning window of the plasmon resonance. The applied bias voltages are chosen such as to stay well within the electrical window of the ionic liquid from -3.5 to 3.0 V. (b) Extracted change in absorption at -3.0 V with respect to the absorption at 0 V.*

6) Millimeter-scale spatial coherence from a plasmon laser

Coherent light sources have been demonstrated based on a wide range of nanostructures, however, little effort has been devoted to probing their underlying coherence properties. Here, we report long-range spatial coherence of lattice plasmon lasers constructed from a periodic array of gold nanoparticles and a liquid gain medium at room temperature (**Figure 12**). By combining spatial and temporal interferometry, we demonstrate millimeter-scale (~1 mm) spatial coherence and picosecond (~2 ps) temporal coherence (**Figure 13**). The long-range spatial coherence occurs even without the presence of strong coupling with the lattice plasmon mode extending over macroscopic distances in the lasing regime. This plasmonic lasing system thus provides a platform for understanding the emergence of long-range coherence from collections of nanoscale resonators and points toward novel types of distributed lasing sources.

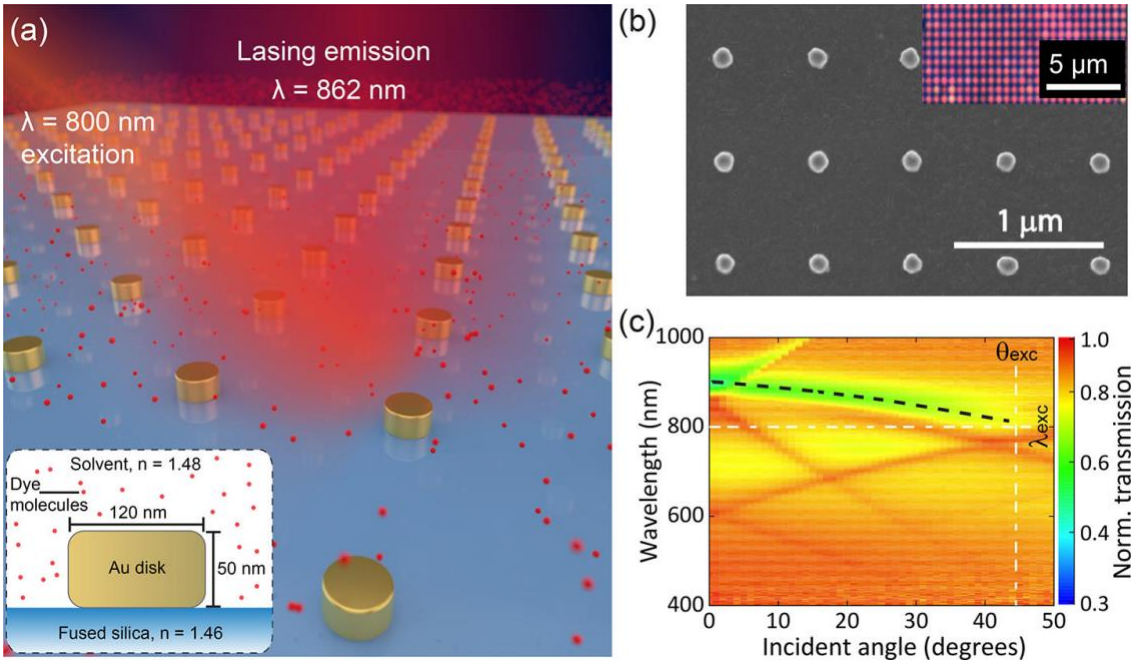

Figure 12. Plasmon nanolaser. *(a) Illustration of the nanoparticle array laser with the excitation beam and emission beam delocalized over many nanoparticles. Inset: Cross-sectional schematic of a single gold nanoparticle surrounded by a solution containing IR-140 dye molecules. (b) SEM image of the gold nanoparticle array. Inset: dark-field optical image of the sample with individual nanoparticles visible. (c) Photonic band diagram measured by angle-resolved transmission for the case with 1 mM IR-140 dye present. The white dashed lines indicate the incident angle and wavelength of the laser excitation. Transmitted light was normalized by the IR-140 dye absorption. The black dashed line is a guide to the eye of the band-edge lattice plasmon that follows the (0, ±1) mode.*

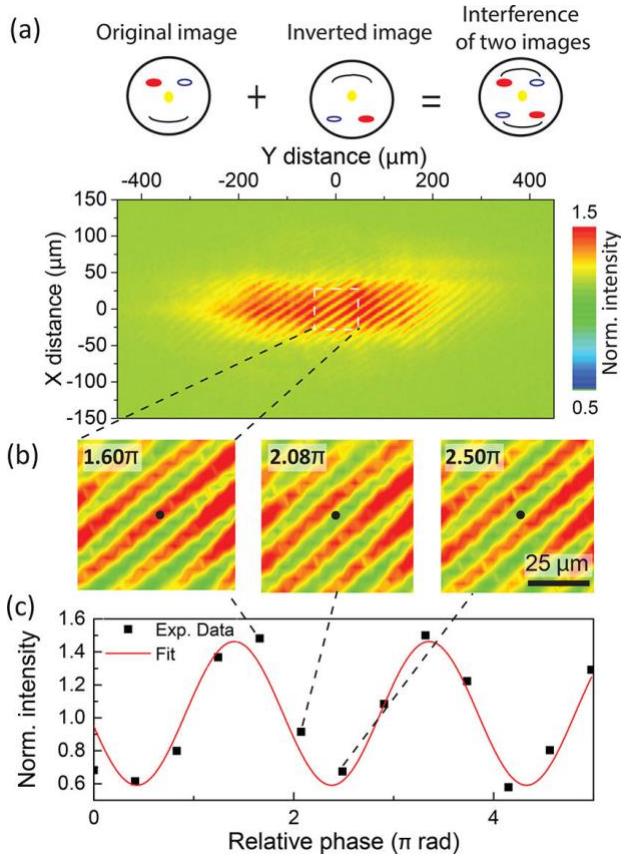

Figure 13. Spatial coherence and visibility. *(a) Top: Illustration of the beam rotation where the real image on one arm of the interferometer was rotated centro-symmetrically after which the two images were overlapped on the camera. Bottom: Real-space image of the interference pattern at an excitation power of P = 1.35 P_{th}. (b) Interferograms from the region indicated by the dashed white line in (a) at different phase delays. The black dot indicates a fixed position on the camera. (c) Interference fringe as a function of the relative phase, showing a contrast of ~45%. The red line is a cosine fit to the data*

7) Tailored emission spectrum of 2D semiconductors using plasmonic nanocavities

Tailoring light−matter interactions in monolayer MoS_2 is critical for its use in optoelectronic and nanophotonic devices. While significant effort has been devoted to enhancing the photoluminescence intensity in monolayer MoS_2, tailoring of the emission spectrum including complex excitonic states remains largely unexplored. Here, we demonstrate that the peak emission wavelengths of the A and B excitons can be tuned up to 40 and 25 nm, respectively, by integrating monolayer MoS_2 into a plasmonic nanocavity with tunable plasmon resonances (see **Figure 14** and **15**). Contrary to the intrinsic photoluminescence spectrum of monolayer MoS_2, we are also able to create a dominant B exciton peak when the nanocavity is resonant with its emission. Additionally, we observe a 1200-fold enhancement of the A exciton emission and a 6100-fold enhancement of the B exciton emission when normalized to the area under a single nanocavity and compared to a control sample on thermal oxide.

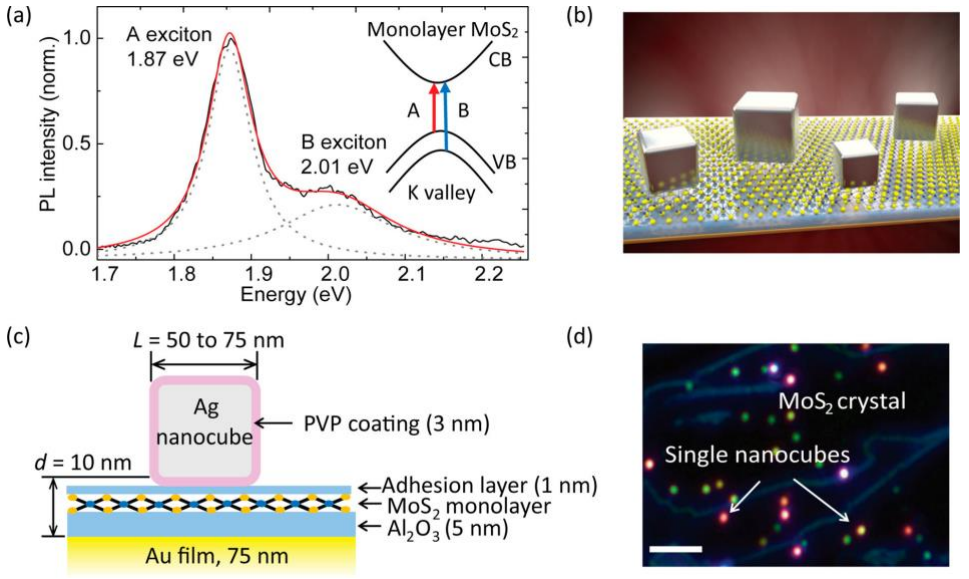

Figure 14. Sample schematic and characterization. *(a) Normalized PL spectrum of monolayer MoS_2 control sample on SiO_2/Si substrate. The measured spectrum (black line) was fitted to A and B exciton peaks at 1.87 and 2.01 eV, respectively (dashed lines). Inset: a schematic band structure of monolayer MoS_2 in the K valley, showing the optical transitions associated with the A and B excitons. CB: conduction band; VB: valence band. (b) 3D illustration of the plasmonic nanocavity, consisting of silver nanocubes of varying sizes on top of a gold film, separated by an Al_2O_3 layer, a MoS_2 monolayer, and a polyelectrolyte adhesion layer. (c) Schematic illustration of the fabricated nanocavity sample. (d) Dark-field microscope image of the fabricated sample. The edges of MoS_2 monolayer appear as the blue outlines and the bright spots represent individual nanocavities. The scale bar is 5 μm.*

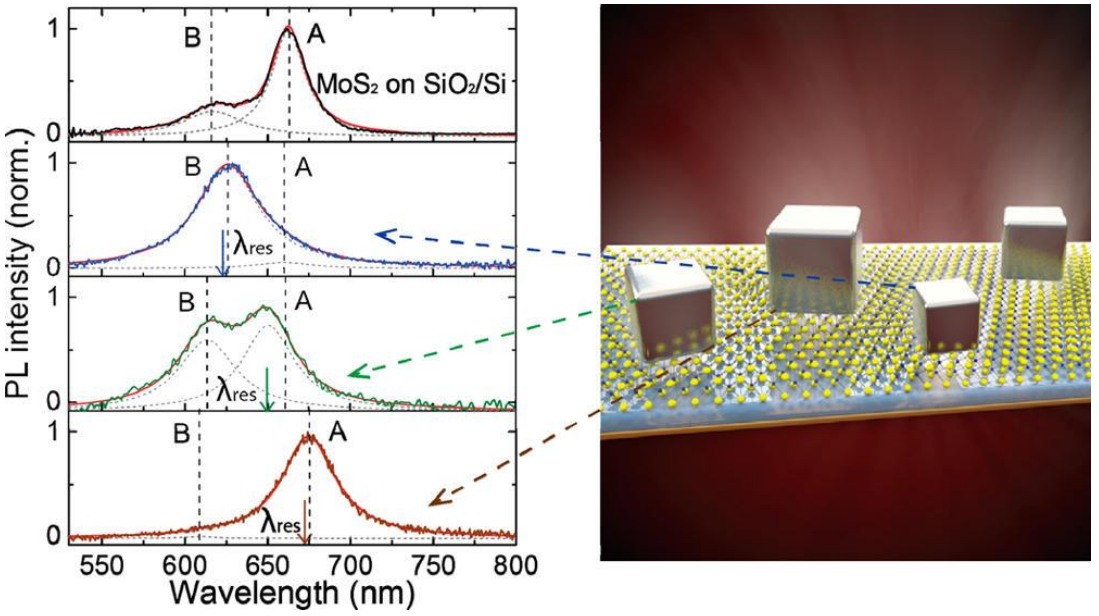

Figure 15. Modification of monolayer MoS_2 emission spectrum. *(a) Shifted PL emission peaks relative to the control sample when monolayer MoS_2 is coupled to nanocavities with varying resonances. The plasmon resonance (λ_{res}) for each individual nanocavity is indicated by the arrow in each panel. Each PL spectrum is fitted to two Lorentz-shaped peaks (dashed gray lines), correlating to the A (at lower energy) and B (at higher energy) exciton peaks. The top panel is a measured PL spectrum of a MoS_2 monolayer on the SiO_2/Si substrate as a reference.*

8) Surpassing Single-Linewidth Active Tuning with Photochromic Molecules Coupled to Plasmonic Nanoantennas

Active plasmonic nanostructures with tunable resonances promise to enable smart materials with multiple functionalities, on-chip spectral-based imaging and low-power optoelectronic devices. A variety of tunable materials have been integrated with plasmonic structures, however, the tuning range in the visible regime has been limited to less than the line width of the resonance resulting in small on/off ratios. Here we demonstrate dynamic tuning of plasmon resonances up to 71 nm through multiple cycles by incorporating photochromic molecules into plasmonic nanopatch antennas (**Figure 16**). Exposure to ultraviolet (UV) light switches the molecules into a photoactive state enabling dynamic control with on/off ratios up to 9.2 dB and a tuning figure of merit up to 1.43, defined as the ratio between the spectral shift and the initial line width of the plasmonic resonance. Moreover, the physical mechanisms underlying the large spectral shifts are elucidated by studying over 40 individual nanoantennas with fundamental resonances from 550 to 720 nm revealing good agreement with finite-element simulations.

The main switching mechanism is a change in refractive index in the gap which, in turn, modifies the plasmon resonance. For certain wavelengths, a resonant coupling between the plasmon resonance and the MC also appears – actually later going into a strong coupling regime (not shown here). We have also started to embed quantum dots into these structures such that the radiative processes of these can be actively controlled – as I previously showed that spontaneous emission rate and PL depend strongly on the plasmon resonance.

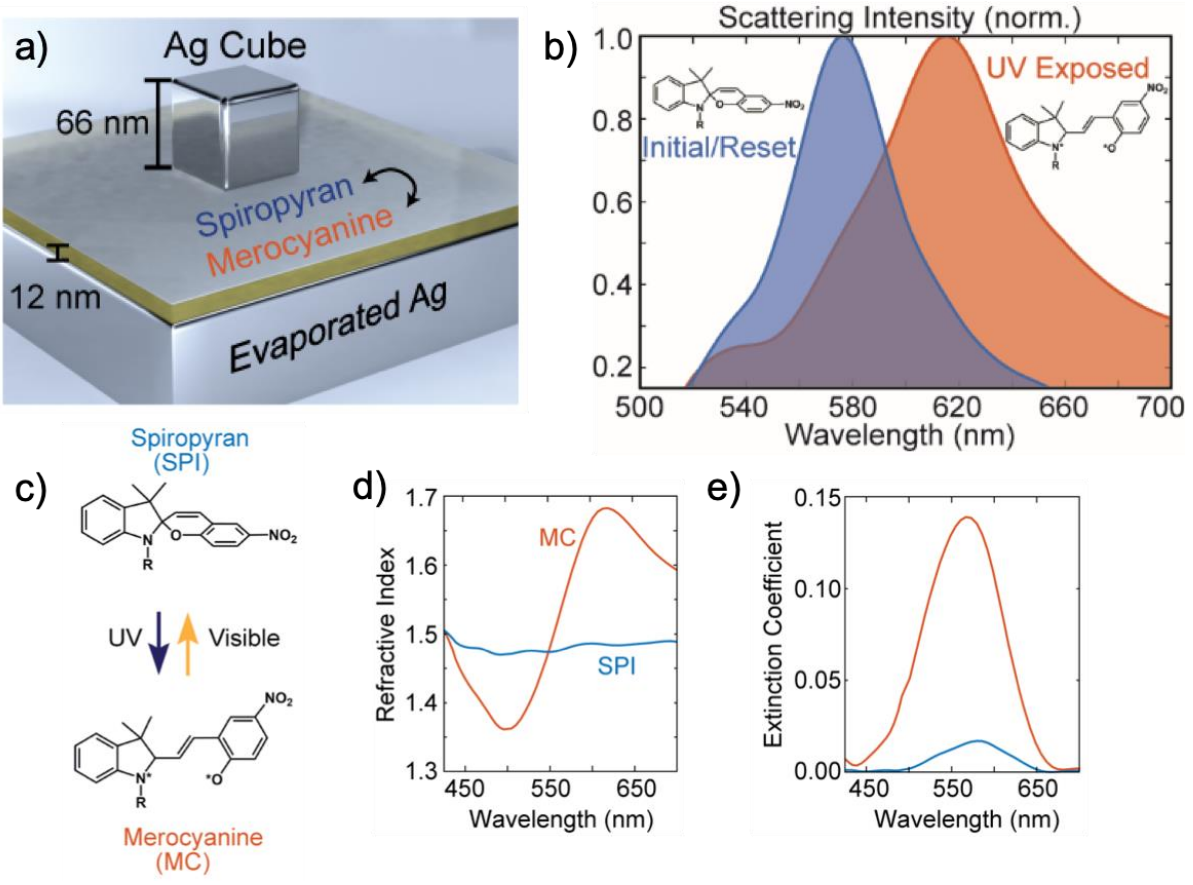

Figure 16. Dynamic tuning with photochromic molecules. *(a) Schematic of film coupled nanopatch antenna with 66 nm nanocube and 12 nm photochromic spacer layer over a 75 nm silver film. (b) Representative scattering spectrum from an individual nanocavity before and after UV exposure demonstrating dynamic and reversible tuning. (c) Chemical structure diagram showing two isomers of spiropyran (SPI) that can be alternated through either UV or visible light exposure. (d,e) Refractive index and extinction coefficient of a 12 nm layer of SPI/PMMA before (blue "SPI") and after UV exposure (red "MC").*

9) Highly-efficient third-harmonic generation in plasmonic nanogaps

Plasmonic structures can precisely localize electromagnetic energy to deep subwavelength regions resulting in significant field enhancement useful for efficient on-chip nonlinear generation. However, the origin of large nonlinear enhancements observed in plasmonic nanogap structures consisting of both dielectrics and metals is not fully understood. For the first time, here we probe the third harmonic generation (THG) from a variety of dielectric materials embedded in a nanogap plasmonic cavity (**Figure 17**). From comprehensive spectral analysis of the THG signal, we conclude that the nonlinear response results primarily from the dielectric spacer layer itself as opposed to the surrounding metal. We achieved a maximum enhancement factor of more than six orders of magnitude compared to a bare gold film, which represents a nonlinear conversion efficiency of 8.78×10^{-4}%. We expect this new insight into the nonlinear response in ultrathin

gaps between metals to be promising for on-chip nonlinear devices such as ultrafast optical switching and entangled photon sources.

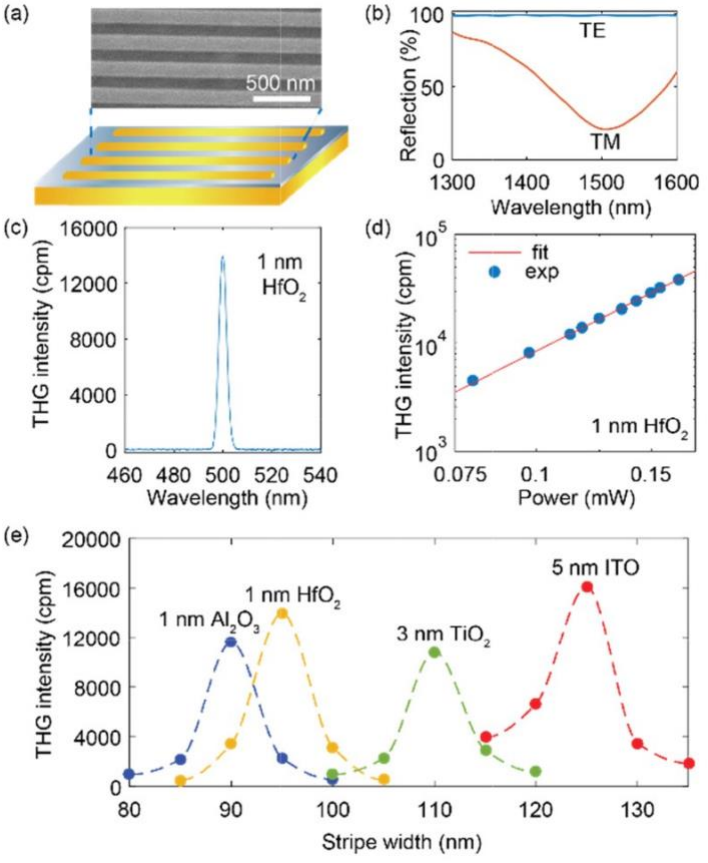

Figure 17. Plasmonic nanogaps for efficient nonlinear generation. *(a) Schematic and SEM image of the sample structure consisting of a thin dielectric layer sandwiched between a gold film and stripes. (b) Measured reflection spectra from an array of stripes for an incident polarization perpendicular to the stripes (transverse magnetic (TM)) and parallel to the stripes (transverse electric (TE)). (c) Representative spectrum of THG from 95 nm stripes for TM polarization. (d) THG intensity from stripes as a function of excitation power confirming a third order power dependence. (e) Dependence of THG intensity on the width of the gold stripes for four different dielectric spacers as indicated in the figure. Dots represent experimental data and dashed lines are guides to the eye.*

10) Review article on "Extreme nanophotonics in ultrathin metallic junctions" in Nature Materials

Wrote review article to disseminate this new interesting field and our recent results to the scientific community.